

Guidelines for standard operation of imaging modalities in orbital diseases (2024)

Yi Shao¹, Jian-Min Ma², Xiao-Ming Huang³; Expert Workgroup of Guidelines for the use of imaging equipment in orbital diseases (2024); Ophthalmic Imaging and Intelligent Medicine Branch Chinese Medicine Education Association; Ocular Oncology Committee of the Ophthalmology Branch of the Chinese Medical Doctor Association; Ophthalmology Committee of International Association of Translational Medicine; Chinese Ophthalmic Imaging Study Groups

¹Department of Ophthalmology, Shanghai General Hospital, Shanghai Jiao Tong University School of Medicine, National Clinical Research Center for Eye Diseases, Shanghai 200080, China

²Beijing Tongren Hospital Affiliated to Capital Medical University, Beijing 100005, China

³Sichuan Eye Hospital, Chengdu 610047, Sichuan Province, China

Correspondence to: Yi Shao. Department of Ophthalmology, Shanghai General Hospital, Shanghai Jiao Tong University School of Medicine, National Clinical Research Center for Eye Diseases, Shanghai 200080, China. freebee99@163.com; Jian-Min Ma. Beijing Tongren Hospital Affiliated to Capital Medical University, Beijing 100005, China. jmma@sina.com; Xiao-Ming Huang. Sichuan Eye Hospital, Chengdu 610047, Sichuan Province, China. eyehxm@126.com

Received: 2024-04-24 Accepted: 2024-07-26

Abstract

• Orbital disorders include conditions originating from the orbital bones, surrounding tissues, and post-orbital septum. They also include systemic ailments affecting the orbit. Different clinical symptoms make up the complex range of orbital disorders. Because these disorders mostly impact the orbital area instead of the intraocular compartment, there is little diagnostic usefulness for typical ophthalmic visual tests. As such, the vital instruments for diagnosing and evaluating orbital illnesses have become ophthalmic imaging modalities, including ocular ultrasonography (B-scan), computed tomography (CT), and magnetic resonance imaging (MRI). One way to improve the precision and promptness of diagnosing orbital diseases is to standardize the functioning of widely used imaging equipment and define the radiological features of orbital abnormalities. Such programs are crucial for the care of patients with orbital disorders since they considerably

reduce the number of misdiagnoses and missed diagnoses in these individuals. The underlying concepts, operational techniques, and normal and pathological imaging findings associated with common diagnostic tools for orbital illnesses are all thoroughly reviewed in this guideline. The objective is to improve primary healthcare settings' diagnostic competence in the field of orbital pathology and to standardize procedures for diagnosing orbital disorders.

• **KEYWORDS:** orbital disease; ultrasonography; computed tomography; magnetic resonance imaging; standardized operation

DOI:10.18240/ijo.2025.01.06

Citation: Shao Y, Ma JM, Huang XM, *et al.* Guidelines for standard operation of imaging modalities in orbital diseases (2024). *Int J Ophthalmol* 2025;18(1):51-66

This article was first reported in the *Guoji Yanke Zazhi (Int Eye Sci)* 2024;24(2):171-181.

International Practice Guidelines Registration: <http://www.guidelines-redistry.cn/>, IPGRP-2023CN487.

INTRODUCTION

Orbital diseases encompass a wide variety of conditions involving the bony orbit, intra-orbital structures, periorbital soft tissues, and even those that are secondary to systemic diseases. A comprehensive analysis conducted in 2021 highlighted the prevalence of various orbital pathologies: thyroid-related eye disease at 30.7%, orbital tumors at 26.6%, trauma accounting for 20.1%, inflammatory conditions at 19.4%, and a combined 3.2% for vascular malformations, congenital, hereditary diseases, and others^[1]. The clinical presentations of these diseases are multifaceted and intricate, with many patients exhibiting symptoms such as reduced visual acuity or ocular redness and pain, which can lead to misdiagnosis as retinal disorders or conjunctivitis, resulting

in missed opportunities for optimal treatment^[2]. However, since the 1970s, rapid advancements in ophthalmic imaging have resulted in significant improvements in diagnostic accuracy, bringing increased attention to orbital pathologies. The inherent characteristic changes seen in most ophthalmic diseases can be distinctly identified through imaging, thus the diagnosis and treatment of these conditions heavily rely on radiological investigations. In the formation of this guideline, there was extensive deliberation on the application of radiological techniques in orbital diseases, analyzing current challenges and potential advancements. The drafting process saw contributions from a team of expert writers, subsequent reviews *via* email and WeChat by other specialists, followed by further iterations, discussions, and consensus-building through online meetings. After a meticulous period of over a year, this guideline offers comprehensive details on imaging principles, methodologies, normal and pathological imaging findings, with the primary aim of standardizing imaging processes, elevating the diagnostic acumen of primary care physicians, and enhancing the overall diagnostic efficacy for orbital diseases.

Ultrasonography Ultrasonography employs the reflective properties of sound to generate images, offering insights into anatomical structures and pathological alterations.

Principles of ultrasonography When an elastic object oscillates, it induces waves in its surroundings that propagate outwardly. This propagated energy is termed ‘sound’. The oscillations per second of the sound source are its frequency, expressed in Hertz (Hz). The diagnostic frequency for orbital diseases ranges between 7.5-10 MHz. Sound’s transmission through a medium encounters’ resistance, termed acoustic impedance. The greater the difference in impedance between two mediums, the greater the energy reflected, resulting in a stronger echo received by the transducer. Utilizing this phenomenon allows for accurate measurements of biometric parameters in various tissues, such as the thickness of ocular structures, axial length, and the refractive power of intraocular lens^[3-6]. Furthermore, as ultrasound traverses different mediums, it undergoes absorption, scattering, reflection, *etc.*, with a portion of its energy being lost as heat, termed “ultrasonic attenuation”. Pathological tissues generally have a higher attenuation than normal tissues. The degree of attenuation in normal tissues follows the order: bone>fibrous tissue>muscle>fat>liquid. Pathological tissues also exhibit varying degrees of attenuation, such as solid lesions having a greater attenuation than liquid-filled cysts. Observing these attenuation patterns aids in qualitative diagnosis.

Classification of ultrasonic modalities Eye care clinics routinely employ several ultrasonographic instruments based on image representation modalities, namely A-mode ultrasound

(A-mode), B-mode ultrasound (B-mode), ultrasound bio-microscopy (UBM) and D-mode ultrasound (D-mode).

1) A-mode In this mode, the probe is strategically placed anterior to the object of interest. As the ultrasonic beam moves forward, reflections arise at every interface encountered. These reflections manifest as wave crests on the baseline, ordered by their time of reflection. These one-dimensional images have the wave crest amplitude indicative of the ultrasonic beam strength; a more intense echo is denoted by a higher crest.

2) B-mode B-mode facilitates visualization of the anatomical structure by converting the echo into a series of luminous points. The brightness of these dots correlates with the intensity of the echo, growing brighter with stronger echoes. Two principal B-mode probes are prevalent in ophthalmological assessments: the mechanically driven fan-scan probe and the line array probe. The former, driven by a motor, yields real-time fan images. The latter utilizes an array of transducers situated within the probe, which, when sequentially activated via an electronic switch, generate images. Clinically, the sector scanning approach, employing the more compact fan-scan probe, is often preferred due to its enhanced resolution relative to the line array method.

3) UBM Introduced into ophthalmic practices in the 1990s^[7-9], UBM stands as a superior imaging modality. Utilizing 35-100 MHz ultrasound waves, enables meticulous examination of intraocular tissues. The enhanced sensitivity of UBM provides real-time monitoring of microstructural intraocular changes. However, given its ultra-high frequency, its penetrative capacity is limited, restricting its examination mainly to anterior eye segments.

4) D-mode D-mode, also known as doppler ultrasound, requires the placement of the probe anterior to the tissue while emitting ultrasound at a fixed frequency. Any relative movement between the probe and tissue alters the echo frequency, a phenomenon termed “frequency shift”. This shift, detectable and quantifiable, is depicted as a color flow map and a spectrogram. The detected frequency change is proportional to the motion velocity, such as blood flow. An increased frequency is noted with blood flow directed towards the probe, while a decrease is observed when directed away. Thus, the frequency shift offers insights into blood flow direction, speed, and overall vascular health.

5) Three-dimensional ultrasound During the 1970s and 1980s, pseudo-three-dimensional ultrasounds were utilized in ophthalmology. This modality merged one-dimensional and two-dimensional images to emulate a three-dimensional perception, albeit without significant diagnostic benefits, and has since fallen out of favor. Recently, genuine three-dimensional images constructed *via* 180° scans accurately depict three-dimensional scenarios. They have been utilized

to showcase retinal detachments, offering certain advantages over two-dimensional images. However, their pragmatic utility warrants further exploration.

Probing methods Diverse clinical objectives necessitate the adoption of various examination approaches. Taking the B-mode sector scan as an exemplar, this discussion aims to differentiate between the direct contact method (used for ocular pathology) and the indirect method (employed for biometric measurements).

1) Direct contact method Instruct the patient to gently close their eyes. Apply a generous amount of coupling agent to the eyelid, and position the probe centrally over the upper eyelid to acquire the image. Maneuver the probe horizontally and rotate it, allowing a comprehensive sagittal scan of the entire eyeball and orbit. Then, orient the probe transversely, and move vertically to complete a coronal scan. After lesion localization, conduct a meticulous examination from varied angles and positions. For intraocular lesions, the eyeball and probe must move in opposing directions to inspect the peripheral regions. If the lesion is localized in the eyelid or orbit, directly position the probe over the corresponding skin. Ensure sensitivity adjustments are made in real-time during the examination, or freeze the image for subsequent processing.

Special techniques may be required for certain pathologies: a) Post-movement examination: After identifying an intraocular lesion, allow eyeball movement and subsequently assess the mobility of the lesion to ascertain its relationship with the ocular wall. b) Compression test: Apply pressure to the eyeball following the detection of an orbital lesion to determine lesion consistency, helping to differentiate vascular from solid or cystic lesions. c) Magnetism test: Essential for intraocular foreign bodies to establish their magnetic nature, which is pivotal for surgical approach decisions. d) Extraocular muscle examination: Extraocular muscles appear as hypoechoic bands. Rotate the eyeball and incline the probe contralaterally to locate the muscle insertions.

2) Indirect examination method This method largely mirrors the direct contact technique but necessitates a water immersion bath in front of the eye. The probe, submerged in saline, should be placed 0.5-1.0 cm away from the eyeball, making it apt for anterior segment lesions

Normal ultrasound images

1) Normal A-mode ultrasound image The typical A-mode image is one-dimensional. Starting from the leftmost baseline, echoes corresponding to the anterior and posterior lens surfaces are discernible at around 6 and 10 mm. A subsequent flat section represents the anechoic vitreous. Roughly 23 mm after the initial wave, the vitreoretinal interface is apparent, followed by varying post-ocular soft tissue echoes. The terminal high-

amplitude spike echoes the bony orbit. The span from the retina to this bony echo generally doesn't exceed 18 mm.

2) Normal B-mode ultrasound images Standard B-mode images may differ based on the probe used and the area visualized. Axial scans with a sector probe may reveal a curved echogenic band representing the posterior lens surface and disc-shaped artifacts from internal reflections. The vitreous, devoid of sound-reflecting interfaces, appears hypoechoic. On the right, a curved echogenic band represents the ocular wall (retina, choroid, and sclera). The W-shaped echoes posteriorly denote post-ocular structures with a central anechoic triangle representing the optic nerve. Off-axis scans might not display the lens echo, and the posterior echoes appear triangular.

3) Normal D-mode ultrasound images For the standard D-mode image, an initial B-mode assessment is essential to rule out pathologies that could affect the vasculature. The color Doppler was engaged to visualize blood flow. The red color suggests flow towards the probe, while the blue color indicates flow away. The brightness of these colors offers a rough speed estimate; brighter colors signify rapid flow. The ophthalmic artery, situated about 15-20 mm posterior to the eyeball and below the optic nerve, usually travels anteriorly, curving above the optic nerve. The ophthalmic artery exhibits vibrant linear bands of red, pulsatile and shimmering, with a blood column diameter ranging between 1 and 1.5 mm. Employing pulsed Doppler imaging, a spectral waveform is delineated, wherein the ultrasound beam's orientation approximates a parallel alignment to the blood flow direction, with a sampling volume set between 0.5 and 1.0 mm³. The spectral profile of the ophthalmic artery reveals a distinct triphasic morphology, characterized by three peaks interceded by two troughs. Based on this spectral representation, key hemodynamic parameters, including blood flow velocity during various phases of cardiac activity, ejection fraction, resistance index, and pulsatility index, are ascertainable. Positioned approximately 10 to 15 mm posterior to the eyeball are the posterior ciliary arteries. They are situated on both the medial and lateral aspects of the optic nerve and maintain a parallel orientation relative to it, presenting a bright red flow. The spectral waveform of these arteries maintains the triphasic pattern aforementioned. Meanwhile, the central retinal artery, localized at the interface of the scleral wall and the optic nerve, within a more shaded region, manifests a fine red flow. Its spectral waveform distinctively assumes a triangular shape.

Abnormal ultrasound images

1) Thyroid-associated ophthalmopathy (TAO)

a) Steps of B-mode ultrasound examination The examinee is placed in supine position with both eyes looking straight ahead, the probe of the ultrasound diagnostic instrument is placed on the opposite side of the extraocular muscle to

be examined, and along the direction of the muscle, the extraocular muscle is scanned horizontally and vertically for morphology and length, scanning the stop-end of the muscle, anterior segment, muscle belly, and posterior segment in order, and selecting the thickest place for measurement to take the value, and recording the soft-tissue echoes, and completing the scanning of the four rectus muscles with the same operation^[10].

b) Imaging features TAO is characterized by the widening of the muscle belly, with thickening of the brow and intraorbital fat pads of the affected eye, while the tendons are rarely involved (Figure 1A). The internal structure of extraocular muscles is hypoechoic and heterogeneous due to muscle inflammatory edema in the active phase, and hyperechoic due to extraocular muscle fibrosis in the resting phase^[11]. However, patients with TAO without thickening of the extraocular muscles can also be seen in the clinic, and therefore the diagnosis of the disease needs to be supplemented with ocular prominence and other imaging tests. It has been shown that after 3mo of treatment for patients with TAO, the thickness of the extraocular muscles and the retrobulbar fat tissue were significantly thinner and slightly more echogenic.

c) Differentiation from extraocular myositis The ultrasound image of extraocular myositis is characterized by an overall widening of the muscle, with internal structures that are hypoechoic and homogeneous, especially in the acute phase, with very low echogenicity^[12].

2) Abnormalities in ocular orbit ultrasonography

a) Space-occupying lesions These can be benign and inflammatory. Benign ones typically appear somewhat round with clear boundaries, surrounded by an inner echo halo, with a uniform distribution of inner echoes. Inflammatory and malignant lesions often have irregular shapes, indistinct or rough boundaries, and an uneven distribution of inner echoes. Upon probing, the eye or tumor might deform if cystic and remain unyielding if solid. Liquid-containing lesions exhibit minimal acoustic attenuation, while fibrous sclerosing lesions manifest higher attenuation. Anechoic lesions predominantly represent liquid masses, including simple cysts, hematomas, abscesses, mucinous cysts, and meningoceles. Hypoechoic lesions are common in optic glioma, schwannoma (Figure 1B), sarcoma, inflammatory pseudotumor, and infantile hemangioma. Moderate echo lesions encompass conditions like pleomorphic adenoma of the lacrimal gland and epidermoid cysts (Figure 1C). Hyper-echoic lesions pertain primarily to calcifications, evident in conditions such as meningiomas invading the orbit from sphenoid bone or vascular calcifications.

b) Morphologic changes in normal structures Enlarged extraocular muscles may be attributed to the inflammation in orbit-specific or inflammatory pseudotumor and TAO.

Thickened optic nerve is often due to meningioma, glioma, or inflammation. A dilated superior ophthalmic vein with pulsations hints at a carotid-cavernous fistula (Figure 1D). Enlarged eyeballs can result from high myopia or alterations post-silicone oil removal. Effusion of the fascial sac of the eyeball is indicated by a crescentic anechoic area exterior to the eyeball wall and a T-sign at the optic nerve, frequently observed in cases of intraorbital inflammation, hemorrhage, or malignant tumors.

3) Abnormal D-mode ultrasonography Abnormal D-mode ultrasound mainly shows abnormal changes and vascular hyperplasia of normal blood vessels. Intraorbital space-occupying lesions may demonstrate color blood flow associated with vascular formation. Refer to the Alder semi-quantitative blood flow grading method for blood flow grading^[13]: Grade 0 is no blood flow seen in the lesion; Grade I is a small amount of blood flow, with 1 to 2 punctate or short rod-shaped blood flow signals visible in the lesion; Grade II is a moderate amount of blood flow, with 3 to 4 punctate blood flows or a blood vessel with a length close to/exceeding the radius of the tumor seen in the lesion; Grade III is a rich blood flow, with 5 or more punctate blood flows or 2 longer blood vessels visible; Grade 0 to I is the non-rich type, and Grade II to III is the rich type. Accordingly, they can be categorized into vascular-rich tumors (malignant tumors), vascular-poor tumors (meningioma), and avascular tumors (cavernous hemangioma, venous hemangioma and dermoid cyst; Figure 2A). Carotid-cavernous fistula manifests as an enlarged superior ophthalmic vein exhibiting either red blood flow or a combination of red-blue blood flow (Figure 2B, 2C).

Computed Tomography Examination Computed tomography (CT) employs X-rays as the energy source to generate cross-sectional two-dimensional images, assisted by computational algorithms. Invented by Hounsfield, this technology gained widespread clinical application in the 1970s and has since evolved to provide three-dimensional imaging capabilities. The penetrating X-ray source allows not only the visualization of soft tissues but also renders skeletal structures with exceptional clarity, often outperforming B-mode ultrasound in lesion delineation and qualitative diagnosis.

CT imaging principle In the CT process, an X-ray tube emits a beam that traverses the patient's head and is captured by detectors situated on the opposite side. These components are mounted on a gantry that rotates 180° around the patient's head, collecting sufficient X-ray attenuation data for subsequent computational reconstruction. Each pixel in the reconstructed image represents a specific density value arranged in a matrix, which is then converted from digital to analog format for display^[14-15]. The attenuation of X-ray energy is directly proportional to tissue density, rendering computed

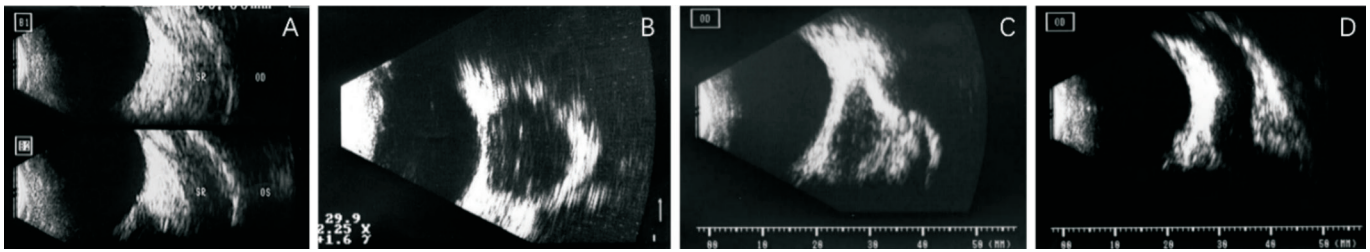


Figure 1 Abnormal ultrasound images A: Thyroid-related ophthalmopathy B ultrasound shows extraocular muscle thickening; B: Schwannoma B-ultrasound shows retrobulbar hypoechoic mass shadow; C: Dermoid cyst B ultrasound shows a retrobulbar medium echoic mass; D: Carotid-cavernous fistula B ultrasound shows thickening of the supraocular vein.



Figure 2 Abnormal D-mode ultrasonography A: Dermoid cyst D-mode ultrasound shows no blood flow signal; B, C: Carotid-cavernous sinus fistula D-mode ultrasound shows thickening of the supraocular vein with red or red-blue blood flow.

CT essentially a density-based imaging modality. To quantify these densities, a Hounsfield unit (HU) scale, spanning a range from air to cortical bone, has been standardized to 2000 HU. Using water as the reference standard with a CT value of 0 HU, tissues with densities lower than water bear negative values, while those denser register positive values. For instance, air is designated a value of -1000 HU, while cortical bone is pegged at +1000 HU. Adipose tissue, possessing a density less than water, falls within the range of -90 to -100 HU. Other soft tissues, inclusive of muscle, nerve fibers, fibrous tissues, vitreous body, and the crystalline lens, typically oscillate between +10 and +80 HU. Within the CT imaging spectrum, density gradients are depicted in shades of gray: higher CT values result in brighter white intensities, such as bones appearing in whitish regions^[16]. Conversely, lower CT values yield darker gray or even black representations, akin to the depiction of air. To augment the human eye's discernment of subtle variances across soft tissues, two integral concepts are introduced: the window width and the window level. The former signifies the span of CT values selected for both image representation and visualization. The latter, also termed the window center, denotes the midpoint CT value between the upper and lower bounds of the window width. The window level should ideally correspond to the CT value of the tissue or pathology under scrutiny. For orbital lesion evaluation, the recommended window level ranges from +35 to +50 HU, with a window width between +300 and +500 HU. The judicious selection of window width and level, tailored to specific diagnostic needs, is paramount to obtaining images of maximum clinical relevance.

Imaging protocols

1) Conventional CT scans Scanning is performed in horizontal, coronal, and sagittal shapes. Horizontal level guided by the orbitomeatal line (OM line), which is a line connecting the external canthus to the center of the external ear canal. Scans start 1 cm below this line and proceed upwards, capturing 8 to 14 slices with a thickness of 3 to 5 mm. For precise assessment of the optic nerve and its associated pathologies, imaging slices of 1.5 mm thickness are conventionally employed. If lesions are suspected to be associated with the maxillary sinus or anterior cranial fossa, supplemental scan planes superiorly or inferiorly might be necessitated. Given that the optic nerve's alignment does not run parallel to the OM line—with its anterior segment being positioned lower than its posterior counterpart—it is a common practice in orbital imaging to extend the head posteriorly by 15°, denoted as OM-15°. Alternatively, the reference line drawn between the lower orbital margin and the superior aspect of the external auditory canal, often referred to as the raids bade line (RBL), is employed. Scanning parallel to this line facilitates the inclusion of the lens, optic nerve, and optic canal within a singular plane. To obviate the potential overlay of lesions with bony structures, coronal and sagittal views may be incorporated as supplementary measures. However, reconstructions from slices exceeding 3 mm in thickness may engender image distortions. The patient is instructed to lie down, tilt the head back, and tilt the scanning frame so that the scanning plane is perpendicular to the OM line, and a direct coronal tomography image can be obtained. The quality of the direct coronal image is better than that of the reconstructed image.

2) Contrast-enhanced CT scans To enhance the distinctiveness of specific ocular lesions during CT imaging, the administration of an intravenous CT contrast agent is essential. The contrast medium is mostly water-soluble iodine contrast medium, and the high attenuation of iodine to X-rays makes the lesion appear high-density on CT. The prevailing approach is the bolus intravenous administration, wherein a high-pressure injector swiftly introduces a specified dosage of concentrated iodinated contrast into the vein. Simultaneously, as the contrast circulates to the target organ *via* the bloodstream, CT scanning ensues. When deploying ionic contrast agents, it is imperative to conduct an iodine allergy test. Nonionic contrast media have fewer side effects, but are expensive. Orbital key structures and tumors are enveloped by adipose tissue. The density differential between fat and both the normal structures and tumors is typically substantial, often exceeding +130 HU. Generally, unenhanced CT can discern lesions adequately given this differential. However, for diagnostic clarity of certain lesions or when ascertaining the intracranial spread of a pathology, contrast-enhanced scanning may be indispensable. Lesions, such as hemangiomas, characterized by robust vascularity, exhibit conspicuous enhancement. Conversely, cystic pathologies often either lack enhancement or display peripheral wall enhancement. Schwannomas, on the other hand, frequently portray heterogeneous enhancement, manifesting as a combination of cystic and solid components.

3) Orbital CT scanning protocols^[17-20]

a) Volumetric data acquisition I) Recommended scanner type: High spatial-resolution CT scanners are recommended. II) Patient position and scan baseline: The patient should lie supine, aligned parallel to the RBL. III) Scan extent: Full orbit and any lesions should be covered. IV) Scan parameters: Tube voltage between 100-120 kV, and current between 50-200 mA. Adjust these settings based on the low-dose protocols specific to the scanner model, such as preset noise indices. Slice thickness should be 1-1.5 mm. Pediatric protocols should adhere to low-dose guidelines. V) Reconstruction Algorithms: Including bone algorithm and soft tissue algorithm, it mainly using soft tissue calculation method of recombinant image, with a matrix size of at least 512×512, a bone window range of +3000 to +4000 HU and window level of +500 to +700 HU, a soft tissue window width of +250 to +400 HU and window level of +40 to +60 HU. VI) Reconstruction slice thickness and interval: For post-processing, use the thinnest slices and inter-slice intervals that are smaller than the reconstruction slice thickness. Opt for suitable reconstruction functions. VII) Contrast-enhanced scans: Soft tissue lesions should be subjected to contrast-enhanced scanning. The selection of contrast media should be based on the *Guidelines for the Use of Iodine Contrast Media (2nd Edition)*^[21].

b) Image post-processing Recommend employing bilateral symmetrical multiple planar reformation (MPR) images. The thin-slice reconstructed images should be reformatted in axial and coronal planes. If required, oblique sagittal planes parallel to the optic nerve for both orbits can be reconstructed. For traumatic or bony lesions, focus on images from the bone algorithm; for other lesions, primarily use the soft tissue algorithm. Depending on clinical needs, proceed with three-dimensional reformatting and post-processing, including maximum intensity projection (MIP) and shaded surface display (SSD).

c) CT reorganization protocols for different ocular lesions While reading the images, adapt window settings dynamically according to the observed content.

I) Orbital trauma Axial slice: Reference line is the RBL line, spanning from the superior to the inferior orbital rim. Bone window settings: width: +3000 to +4000 HU, level: +500 to +700 HU. MPR thickness ≤ 2.5 mm and interval ≤ 3.0 mm.

Coronal slice: The reference line is perpendicular to the hard palate, encompassing the anterior orbital margin to the anterior clinoid process. Bone window settings: width: +3000 to +4000 HU, level: +500 to +700 HU. MPR thickness: ≤ 2.5 mm and interval: ≤ 3.0 mm. Soft tissue window settings: width: +250 to +400 HU, level: +40 to +60 HU. MPR thickness ≤ 3.0 mm and interval ≤ 2.5 mm.

Oblique sagittal slice: Reference line parallels the optic nerve, covering the medial and lateral walls of the orbit. Bone window settings: width: +3000 to +4000 HU, level: +500 to +700 HU. MPR thickness ≤ 2.5 mm and interval ≤ 3.0 mm.

II) Non-traumatic orbital lesions Axial slice: Reference line corresponds to the auriculo-orbital line (from the external ear canal to the inferior orbital margin), spanning from the superior to the inferior orbital rim. Soft tissue window settings: width: +250 to +400 HU, level: +40 to +60 HU. MPR thickness ≤ 3.0 mm and interval ≤ 2.5 mm.

Coronal slice: Reference line perpendicular to the hard palate, spanning the anterior orbital margin to the anterior clinoid process. Bone window settings: width: +3000 to +4000 HU, level: +500 to +700 HU. MPR thickness: ≤ 2.5 mm and interval ≤ 3.0 mm. Soft tissue window settings: width +250 to +400 HU, level: +40 to +60 HU. MPR thickness ≤ 3.0 mm and interval ≤ 2.5 mm.

Oblique sagittal slice: Reference line is parallel to the optic nerve, covering the medial and lateral walls of the orbit. Soft tissue window settings: width: +250 to +400 HU, level: +40 to +60 HU. MPR thickness ≤ 3.0 mm and interval ≤ 2.5 mm.

III) Optic nerve canal evaluation Axial slice: The reference line runs parallel to the line connecting the posterior clinoid to the tip of the nasal bone, encompassing the superior and inferior walls of the optic canal. Window settings: width +3000

to +4000 HU, level: +500 to +700 HU. MPR thickness 1.0 mm and interval 1.0 mm.

Coronal slice: The reference line is perpendicular to the auriculo-inferior orbital line, spanning from the orbital apex to the anterior clinoid process. Window settings: width +3000 to +4000 HU, level +500 to +700 HU. MPR thickness 1.0 mm and interval 1.0 mm.

Oblique sagittal slice: The reference line runs parallel to the long axis of the optic canal, covering the medial and lateral walls. Window settings: width +3000 to +4000 HU, level: +500 to +700 HU. MPR thickness 1.0 mm and interval 1.0 mm.

Normal CT images of the orbit Understanding the normative topographical variations in CT imaging is pivotal for accurate diagnosis and treatment planning. While scanning planes and anatomical sites may differ, bilateral symmetry should generally be observed.

1) Axial plane imaging The maximum vertical diameter of the orbit is about 40 mm and the slice thickness is 5 mm, extending from the inferior to superior orbital margin, a total of 8 slices comprehensively encapsulates all intra-orbital structures. For a thickness of 3 mm, 14 slices are required. Depending on necessity, additional slices can be acquired either inferiorly (to include the maxillary sinus) or superiorly (incorporating the orbital roof and anterior cranial fossa floor). Due to the 25° incline of the inferior orbital wall from posterior to anterior relative to the horizontal plane, no single slice can capture its entirety when parallel to either the OM or RBL. The medial orbital wall aligns parallel with the sagittal plane, while the lateral orbital wall demonstrates a 45° angle to it. Consequently, on an axial plane 10 mm below the OM line, only the anterior edge of the inferior wall is visible, excluding intra-orbital soft tissues. A round soft tissue density at the anterior part of the orbital cavity represents the globe at its inferior section. On slices coinciding with the OM line, the orbital cavity retains its cup-shape, with the maxillary sinus forming the cup's base. The lateral wall, primarily constituted of the zygomaticofrontal process and the greater wing of the sphenoid, is relatively thick. An aperture in its posterior section denotes the infraorbital fissure. Transparent regions posteriorly within the orbit, either oval or triangular, are the upper portions of the maxillary sinus. The thinner medial wall is composed of the lacrimal bone and ethmoidal lamina papyracea. An annular soft tissue shadow, termed the ocular ring, represents the globe's inferior section in an axial view. The wedge-shaped shadow between the ocular ring and the top of the maxillary sinus corresponds to the horizontal cross-section of the inferior rectus muscle. If the muscle is hypertrophied, its appearance on this plane can be misinterpreted as an intra-orbital lesion.

The mid-orbital image includes slices 5-10 mm above the OM line. Here, the orbital cavity somewhat resembles a triangle.

The lateral wall is anteriorly thick and posteriorly thin, with its posterior aperture marking the superior orbital fissure. The medial wall, comprised of the lacrimal bone and ethmoidal lamina papyracea, appears as a linear osseous shadow. A circular ocular ring is evident anteriorly within the cavity. The anterior elliptical high-density shadow within the ring represents the lens, the structure with the highest density within the orbit, with a CT value that can reach +80 HU. Soft tissue shadows on both sides of the ocular ring correspond to the medial and lateral canthal tendons. The tubular shadow extending posteriorly and medially from the ocular ring represents the optic nerve. The elongated soft tissue shadows hugging the medial and lateral walls are, respectively, the medial and lateral recti muscles. At the orbital apex, the ophthalmic artery can be seen wrapping around the optic nerve. The interstices among the ocular ring, optic nerve, and extraocular muscles, characterized by low density, denote the locations of intra-orbital fat. A transparent zone medially is the ethmoidal sinus, and laterally outside the lateral orbital wall, the upper part contains the temporal fossa and its embedded soft tissue, with the posterior section housing the temporal lobe of the brain.

Upper orbital images encompass slices 15-25 mm above the OM line. Here, the anterior portion of the orbital cavity varies considerably. On the +15 mm slice, while the cavity retains its triangular shape, the anterior edge of the lateral wall has extended medially. The elongated soft tissue shadow stretching anteriorly from the apex represents the combined superior rectus and levator palpebrae superioris muscles. At times, the superior ophthalmic vein, which courses from anterior to posterior and laterally, turning medially in the mid-orbit to enter the cavernous sinus via the superior orbital fissure, can be seen sandwiched between the optic nerve and the superior rectus muscle. The lacrimal gland is evident on the anterolateral section of the orbit, presenting as an elongated oval soft tissue shadow. Above the orbit lies the frontal lobe of the brain. Visualization of the optic canal necessitates slices of 1.5-3.0 mm thickness, with a window width exceeding 1000 HU. This canal makes a 35° angle with the sagittal plane.

2) Coronal plane images The majority of intra-orbital and peri-orbital anatomical structures are visualized with exceptional clarity in the realm of axial CT. Nevertheless, this approach demonstrates certain limitations, notably in its portrayal of the orbital roof, floor, and the superior and inferior rectus muscles. When oriented in a coronal perspective, the anterior segment of the orbit elucidates the superomedial orbital wall, complemented by the extraocular muscle tendons and the globe's coronal aspect within the orbital cavity. Transitioning to the mid-orbital coronal perspective, the orbital cavity primarily exhibits a circular or elliptical morphology.

Detailed quadrant imaging reveals cross-sectional views of the four rectus muscles, in addition to the superior oblique muscle. A central, medially-offset hyperdense region distinctly represents the optic nerve. Enhanced visualization *via* high-resolution CT brings to the fore intricate structures, including the superior ophthalmic vein, ophthalmic artery, and frontal nerve nestled between the optic nerve and the superior rectus muscle. Within the orbital confines, the low-density regions correspond to adipose tissue depictions. The orbital anatomy further demarcates the medial and superomedial sections as the ethmoidal sinus, frontal sinus, and anterior cranial fossa, respectively. Approaching the orbital apex, the cavity adopts a slightly triangular configuration with an inferolateral deficit signifying the inferior orbital fissure. An intimate spatial relationship between the rectus muscles and the optic nerve becomes increasingly evident deeper within the orbital space, albeit separated by low-density fat layers. Utilizing enhanced scans *via* high-resolution CT magnifies the visualization of finer elements, including motor and sensory nerves, along with the ophthalmic artery and vein. Medially, the orbital boundary is characterized by the posterior ethmoidal sinus, with the superior boundary aligned with the anterior cranial fossa.

3) Sagittal plane image Conventional sagittal plane imaging is suboptimal for delineating the intricate anatomical structures within the orbit. This limitation arises due to the inherent angular orientation of the superior and inferior rectus muscles and the optic nerve relative to the sagittal plane. When a slice orientation deviates by an angle of 25° from the standard sagittal plane, it affords a comprehensive view. This orientation not only elucidates the superior and inferior orbital walls but also offers an unobstructed longitudinal visualization of the optic nerve and the superior and inferior rectus muscles within the orbital confines. The anterior eye ring presents as an oblique cross-sectional view of the globe.

Abnormal CT images

1) Intraocular hyperdense shadows These are predominantly hallmarks of tumors. For instance, retinoblastoma typically manifests on CT scans with either a standard or slightly enlarged globe size, a hyperdense shadow in the vitreous humor's hypo-dense region, diffuse thickening of the ocular ring, partial or complete calcifications within the lesion, and, if extending along the optic nerve, indications of an enlarged nerve and an expanded optic canal. When the disease induces eyeball atrophy, the CT reveals a shrunken ocular volume. Choroidal melanoma showcases a localized thickening of the globe in a mushroom-like configuration, with extrinsic proliferations connected to intra-orbital hyperdense shadows. Meanwhile, choroidal osteomas primarily exhibit bone shadows posterior to the ocular ring.

2) Intraorbital hyperdense shadows High-density

intraorbital lesions predominantly represent radiographic hallmarks of space-occupying pathologies. Benign neoplasms typically manifest as near-circular, well-demarcated, homogenous medium- or high-density lesions. Cavernous hemangiomas, predominantly nestled within the muscle cone, often appear round or near-circular, medium-density mass opacities on imaging, with CT values often surpassing +50 HU, which display significant enhancement, revealing a characteristic progressive intensification upon contrast administration (Figure 3A-3D). Pleomorphic adenomas of the lacrimal gland, sited in the lacrimal fossa, are typically near-circular. Long-standing tumor-induced pressure might lead to local bony attenuation. Dermoid cysts, frequently localized superiorly outside the orbit, are discerned as semi-circular or annular high-density lesions. The heterogeneity in their internal density can encompass negative values or consistently lipid-like densities. Tumor-induced bony defects may manifest as local orbital depression or perforation, occasionally establishing communication with the temporal fossa or cranial cavity. Contrast-enhanced scans typically elucidate annular enhancement of the cystic wall, while the content remains unenhanced. Malignant tumors often present as irregular, ill-defined, non-smooth, and heterogeneous high-density lesions. Bony erosion with potential invasion into adjacent structures is a common finding. Inflammatory masses, including inflammatory pseudotumors, parasitic granulomas, and vasculitides, present on CT as irregular, unevenly-bordered lesions with notable enhancement. When an inflammatory pseudotumor involves the extraocular muscles and ocular wall, there's a radiographic appearance of muscle thickening and an increased thickness of the ocular ring (Figure 3E).

3) Enlargement of extraocular muscles Extraocular muscle enlargement is a prominent feature in both TAO and myositis-type inflammatory pseudotumors. The former is characterized predominantly by bilateral symmetrical orbital involvement or unilateral enlargement of one or multiple extraocular muscles. The inferior rectus muscle is most commonly affected, followed by the medial rectus muscle and the superior rectus muscle, the lateral rectus muscle is rarely affected. The enlarged extraocular muscles are fusiform, mainly with the thickening of the muscle-abdomen, and a few patients may have tendon thickening, orbital apical density, optic nerve thickening, and occasionally lacrimal gland enlargement and ethmoid cardboard compression (Figure 3F, 3G). In contrast, myositis-type inflammatory pseudotumors primarily affect a single muscle or multiple muscles within one orbit. The muscle enlargement observed is irregular, and the muscle-tendon junctions are frequently compromised. To differentiate this from TAO, it is imperative to integrate the patient's thyroid function test results.

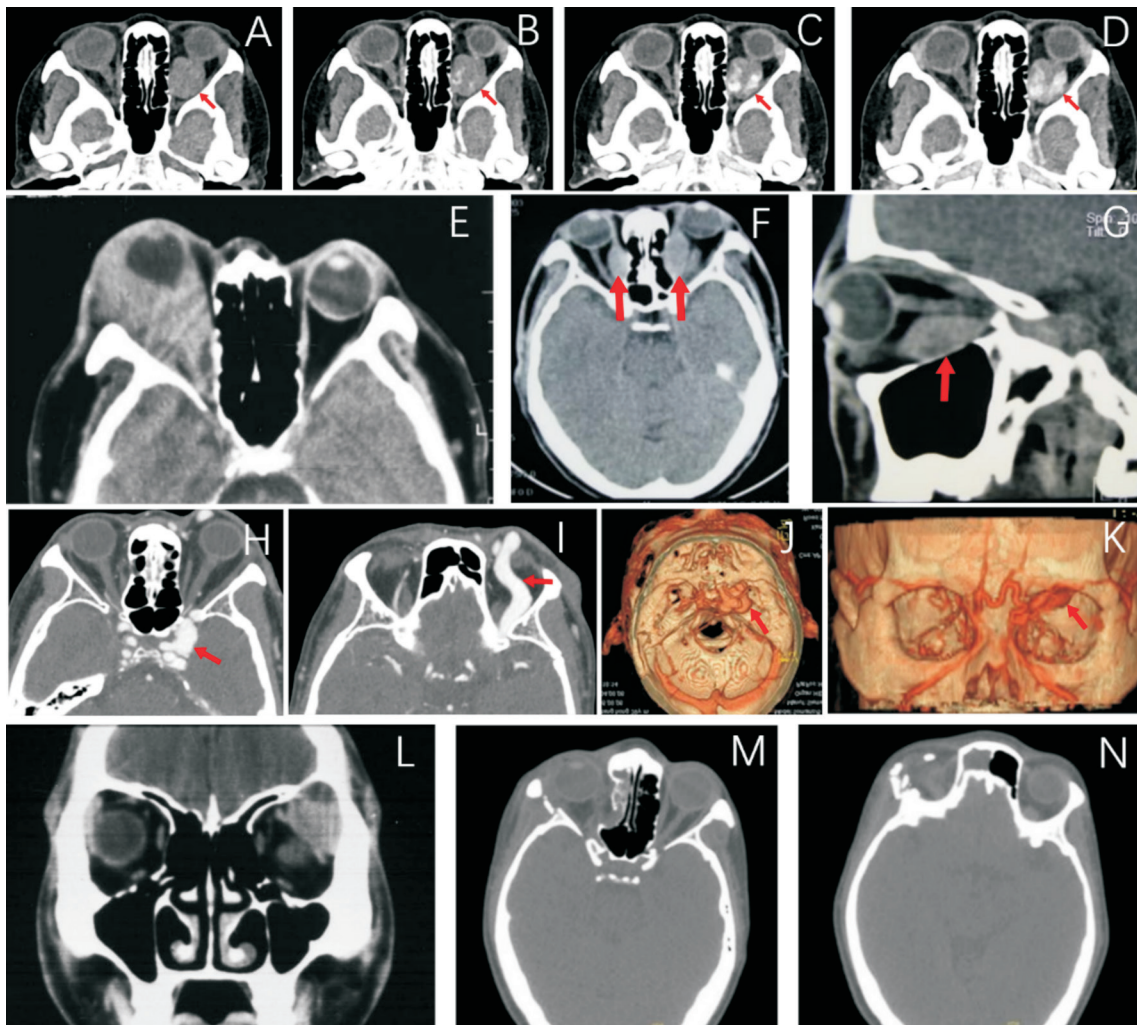


Figure 3 Abnormal CT images A-D: CT of cavernous hemangioma showed a round-like or rounded medium-density mass shadow in the posterior square muscle cone of the left eyeball, showing gradual enhancement and gradual filling (arrowhead); A: Non-contrast image; B: Arterial phase image; C: Venous phase image; D: Delayed image; E: CT of inflammatory pseudotumor showed protrusion of the right eye and thickening of the eye ring; F, G: Grave's ophthalmopathy, CT showing marked thickening of the medial and inferior rectus muscles on both sides, with obvious thickening of the abdomen and no tendon involvement (arrows); H-K: CT internal carotid-cavernous fistula showing protrusion of the left eyeball, widening of the left cavernous sinus, and marked thickening and tortuosity of the left supraocular vein (arrow); L: CT of lacrimal gland mixed tumor showed a medium-density shadow in the left lacrimal gland area; M, N: CT scan of orbital fracture showed multiple comminuted fractures of the right orbital internal, external, and inferior lateral walls, right maxillary sinus, ethmoid sinus, and right zygomatic bone, right optic nerve tortuosity, and right extraocular muscle shape.

4) Thickening of the optic nerve Predominantly seen in conditions like meningiomas, optic nerve gliomas, optic neuritis, and traumatic optic neuropathy. Images of meningiomas show thickening of the optic nerve in a tubular, prismatic, or conical shape, manifesting as a double-track sign, which reaches the eyeball and the neural tube, and may spread intracranially, and may be combined with calcification, which suggests that the tumor is growing slowly. The image of optic nerve glioma shows fusiform thickening of the optic nerve, often with kinking, and enlargement of the optic nerve canal on the side of the lesion^[22].

5) Dilatation of the superior ophthalmic vein The superior ophthalmic vein, on standard CT scans, is observable in approximately 33% of individuals, typically manifesting a

knee-flexion or teardrop morphology (Figure 3H-3K). Such venous dilatation is predominantly seen in carotid-cavernous fistulas and intraorbital arteriovenous malformations. The former, when contrast-enhanced, may display dilation of the ipsilateral or bilateral cavernous sinus. The latter exhibits intraorbital hyperdense lesions. Furthermore, thyroid-associated orbitopathy, due to the enlarged muscles at the orbital apex obstructing venous return, might occasionally also present with superior ophthalmic vein dilatation.

6) Lacrimal gland enlargement Lacrimal gland enlargement is observed in conditions such as lacrimal gland tumors (Figure 3L), inflammatory pseudotumors, and benign lymphoepithelial lesions. Benign tumors of the lacrimal gland typically present as spherical or oval enlargements. In contrast,

malignant variants usually manifest irregular morphologies, often accompanied by bony destruction in the region of the lacrimal fossa. Inflammatory pseudotumors and benign lymphoepithelial lesions predominantly present with uniform enlargement of the lacrimal gland. The former commonly affects one gland, while the latter is often bilateral.

7) Ocular trauma Ocular trauma encompasses soft tissue injuries, fractures, and foreign bodies. Soft tissue injuries may display increased vitreous density, augmented orbital soft tissue volume, and an enlarged optic nerve. Intraorbital hematomas appear as hyperdense lesions, unenhanced by contrast agents. Orbital fractures are mainly categorized as direct, compound, and burst fractures, with fracture lines, bone fragments, and displacements on imaging. Orbital fractures are most commonly fractures of the medial wall, followed by the inferior wall, and CT images show displacement of the rectus muscle and other intraorbital contents. When it combines with contusion of the rectus externus muscle, abnormalities of the paranasal sinuses, and pneumoperitoneum in the orbit, CT images show thickening, deformation, and blurring of the edges of the rectus externus muscle, and effusion in the sieve sinus airspace or soft-tissue shadows^[23] (Figure 3M, 3N). A quintessential blow-out fracture usually manifests with an opening in the infraorbital groove or canal, with soft tissue trapped within the fracture or prolapsed into the maxillary sinus. Clinically, this might present with enophthalmos and limitation in upward gaze. Intraorbital foreign bodies can be categorized as hypo-, iso-, or hyperdense. Metallic foreign bodies, regardless of their location—be it intraocular, within the orbital fat, extraocular muscles, or bone—always appear hyperdense due to the stark density contrast with soft tissues, often producing radiographic artifacts.

Magnetic Resonance Imaging When certain specific atomic nuclei are placed in a magnetic field and stimulated by radiofrequency pulses, these nuclei absorb and then release the pulsed signal, resulting in the formation of cross-sectional images. This process is known as magnetic resonance imaging (MRI). Compared to CT scans, MRI offers a broader range of imaging parameters, superior soft tissue resolution, and lacks the ionizing radiation of X-rays, facilitating multi-directional cross-sectional images. However, its application is contraindicated in individuals with magnetic foreign bodies or implants, as their potential movement within the magnetic field may induce iatrogenic injuries.

Imaging principle Nuclei are composed of protons and neutrons, collectively referred to as nucleons. These nucleons continuously spin about their own axes, generating faint magnetic fields. In nature, the orientation of these spinning axes is random. In nuclei with an even number of nucleons, their respective magnetic fields tend to cancel each other out.

Thus, MRI predominantly employs nuclei with an odd number of nucleons, such as ^1H , ^{23}Na , ^{31}P , and ^{39}K . Given that water constitutes over 60% of the human body and is ubiquitously distributed across tissues—with each water molecule containing two hydrogen atoms—and due to the simplicity of the hydrogen nucleus (consisting of a single proton) with its inherent strong magnetic property, MRI predominantly utilizes hydrogen nuclei for imaging^[24].

When the human body is introduced into a strong magnetic field, the orientation of the spinning protons inside the body changes, gradually aligning parallel to the magnetic lines of force (magnetic field Z-axis). In addition to this spinning movement, these protons also revolve around the Z-axis. Once nucleons achieve a state of equilibrium parallel to the magnetic field lines, applying an external radiofrequency pulse can excite these protons, causing them to rotate about the Z-axis. The angle of rotation increases with the magnitude of the radiofrequency energy; a rotation of 90° is termed a 90° pulse, while a rotation of 180° is known as a 180° pulse. Upon cessation of the radiofrequency pulse, the excited nucleons relax back to their equilibrium state, releasing the absorbed energy as a pulsed signal or MR signal. This signal is spatially localized by gradient coils, captured by receiver coils encircling the body, and subsequently digitized and processed by a computer to form the MRI image. The resulting image is displayed in shades of gray, with high signals appearing bright white, low signals appearing dark black, and intermediate signals appearing gray.

Post radiofrequency pulse, as nucleons transition from their excited high-energy state to a relaxed low-energy state, they undergo a period known as the relaxation time (T). This time is divided into longitudinal relaxation time (T_1) and transverse relaxation time (T_2). Shorter T_1 values result in stronger released energy and, hence, a higher MR signal intensity, whereas longer T_2 values correlate with higher signal intensity. The relaxation times serve as pivotal imaging parameters in MRI. Additionally, proton density and flow dynamics also impact signal strength. Tissues with higher proton density absorb more energy and thus release a stronger MR signal. Rapid arterial blood flow, although absorbing the radiofrequency pulses, often doesn't produce a detectable MR signal due to the gradient coil's inability to capture its release, preventing image formation.

MRI can utilize both 90° and 180° radiofrequency pulses, with differing pulse sequences due to varying sequence orderings. A sequence of continuous 90° pulses is termed a saturation recovery (SR) sequence, primarily illustrating proton density. A sequence starting with a 90° pulse followed by a 180° pulse is known as a spin echo (SE) sequence, optimal for depicting normal structures. Conversely, a sequence initiating with a

180° pulse followed by a 90° pulse is termed an inversion recovery (IR) sequence, which renders pathological changes most effectively. To economize on time while satisfying clinical needs, some protocols employ only the SE sequence but modify the pulse repetition time (TR) and echo time (TE) to derive satisfactory proton-weighted, T₁-weighted, and T₂-weighted images. Additionally, there are fast sequences to shorten imaging times. Recent advancements, aiming to detail specific structures, have led to the development of techniques like magnetic resonance angiography (MRA) and fat suppression, which are employed for specialized diagnostic needs^[25-29].

Examination protocol

1) Scanning scope Complete orbital and lesion encompassment.

2) Coil selection The head coil is typically employed. For specific ocular abnormalities, surface coils can be preferred.

3) Slice thickness and spacing Slice thickness ranges between 3.00 to 5.00 mm, with an inter-slice gap of 0 to 1.00 mm.

4) Pre-scan preparations Patient education is paramount to minimize ocular motion; its control directly influences the quality of the orbital images. Depending on individual comfort, patients can either close their eyes and consciously limit eye movement or fixate on a specific target positioned on the scan framework.

5) Scan sequences Routine scans: standard axial sequences include T₁-weighted imaging (T₁WI) and T₂-weighted imaging (T₂WI), in addition to coronal fat-suppressed T₂WI. If high signal intensities are detected within a mass on T₁WI, consider adding axial fat-suppressed T₁WI and, when appropriate, oblique sagittal sequences as well as diffusion weighted imaging (DWI) sequences^[30-32].

Contrast-enhanced scans: For further tumor characterization, axial dynamic contrast-enhanced scans can be performed, following which a dynamic contrast curve can be plotted. Post-enhancement sequences primarily consist of axial T₁WI with optional coronal or oblique sagittal T₁WI. Select the optimal plane for fat suppression^[33-34].

Pressure scans: In patients exhibiting proptosis upon looking downwards, suspecting venous varix, an initial axial T₂WI sequence should be acquired. Subsequent scans post-neck-cuff inflation are performed following the regular protocol.

Cavernous sinus abnormalities: Adherence to relevant guidelines is advised.

Conventional MRI characteristics The MRI images illustrate tissue structures with congruence to CT in terms of shape, size, and boundaries. However, while CT reflects density, MRI portrays signal intensity. Consequently, gray scale placement differs between modalities. Beyond tissue-specific attributes like T₁, T₂, and fluid dynamics, MR imaging

parameters are influenced by factors such as TR, TE, coil positioning, and paramagnetic contrast agents. Standardizing extrinsic parameters (like TR and TE) is pivotal to maintain a consistent judgment of tissue signal intensity. As delineated below, utilizing a head coil for MRI in a plain scan setting, proton density weighted images (PDWI) adopt a TR/TE of approximately 1500-2000/20-30ms. T₁-weighted images (T₁WI) are characterized by a TR/TE of around 500-600/15-20ms, while T₂-weighted images (T₂WI) present a TR/TE within the range of 2000-2500/190-100ms.

Orbital fat is abundant in hydrogen nuclei with a short T₁ and comparatively longer T₂. On both PDWI and T₁WI, it displays high signal intensities, but T₂WI shows a relative decrease. Both the optic nerve and extraocular muscles have intermediate proton content and relaxation times. Thus, on PD, T₁, and T₂-weighted images, they exhibit moderate signals. Considering the optic nerve's transverse diameter (approx. 3-5 mm), when slice thickness exceeds this value, volume averaging occurs. For instance, with a 5 mm slice thickness, even if the nerve is fully encapsulated, there remains an additional 1.5 mm of fat displaying a much stronger signal intensity. Additionally, chemical shift artifacts (pseudo-images) can cause the fat signal from one side to shift to the opposite side, thereby compromising the depiction of the optic nerve on routine scans. Fat suppression techniques can remedy this by nullifying the fat signal, thereby enhancing the visualization of the optic nerve and extraocular muscles. Bone remains inconspicuous on MR images, free from bone averaging effects, offering a clear view of the intracanalicular segment of the optic nerve. The intracranial segment of the optic nerve, the optic chiasm, and the anterior part of the optic tract are all surrounded by cerebrospinal fluid, appearing as low signal intensities on T₁WI.

Cornea and sclera, primarily comprised of collagen fibers, manifest as low signals on both T₁ and T₂-weighted images due to their long T₁ and short T₂ relaxation times. Choroid and retina, given their thinness, are challenging to distinguish on MRI. On T₁WI, they appear as mid to low signals, while on T₂WI, their signals are slightly elevated. Aqueous humor and vitreous share MR properties with water, exhibiting low signals on T₁WI and high signals on T₂WI. The crystalline lens, contingent upon age and thus varying water content, generally presents a medium signal on T₁WI. On T₂WI, amidst the high signals of aqueous and vitreous, it is discerned as an oval-shaped low to medium signal.

Abnormal MRI findings

1) Intraocular tumors Predominantly, these are choroidal melanomas and retinoblastomas. Choroidal melanomas represent the most common intraocular malignancy in adults. Owing to the substantial melanin content, which exhibits

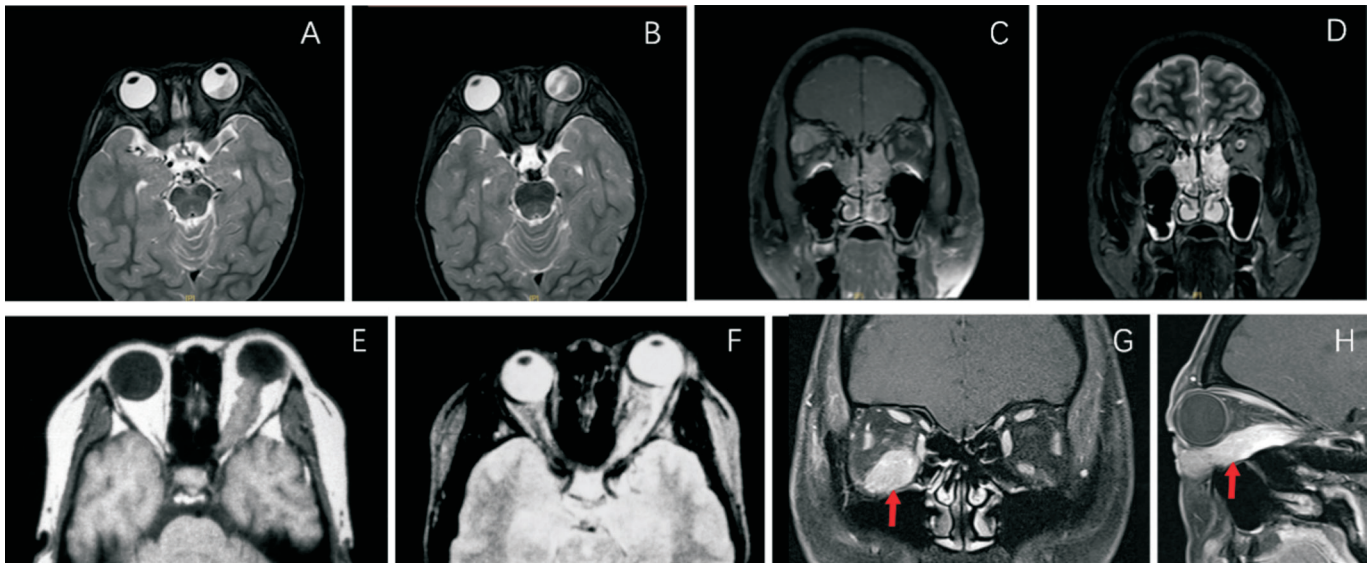


Figure 4 Abnormal MRI findings A, B: MRI images of retinoblastoma showed that the left eyeball was slightly prominent. The lateral posterior inferior area of the left eyeball showed an irregular mass of abnormal signal shadows, T₂WI was mixed and equal, hyperintense, and the enhanced scan was unevenly enhanced, ranging from about 18 mm×17 mm×13 mm, no obvious extrabulbar invasion was found, and the T₂WI optic nerve signal was lower than that of the contralateral side, and the edge was blurred. C, D: MRI image of lacrimal gland mass. C: Moderate enhancement of the lesion. The eyeball is displaced downward, protrusion, and the lacrimal gland fossa is enlarged, and the bone structure is not significantly damaged; D: T₂ weighted scan, and a lobulated space-occupying lesion can be seen in the lacrimal gland fossa outside the upper quadrant muscle cone outside the right orbit, and the range is about 23 mm×34 mm. T₂WI is hyperintense. E, F: MRI image of meningioma. E: T₁ weighted scan showing thickening of the optic nerve in the left eye; F: T₂ weighted scan showing hyperintensity. G, H: Inflammatory pseudotumor MRI shows obvious thickening and swelling of the rectus muscle under the right eye, hyperintensity in the active phase of T₂, and tendon attachment point involved (arrow).

paramagnetic properties, these tumors display a hyperintense signal on T₁-weighted images (T₁WI) due to the shortened T₁, while presenting as hypointense on T₂-weighted images (T₂WI) because of the reduced T₂. However, amelanotic melanomas lack this distinct imaging characteristic. On the other hand, retinoblastoma stands as the most prevalent intraocular tumor in children. Being devoid of melanin, it manifests a moderate signal intensity on T₁WI and a high intensity on T₂WI. Intratumoral calcifications, inherently devoid of MR signal, interspersed within the tissue can lead to irregular hypointense areas on both T₁ and T₂-weighted images, serving as a diagnostic hallmark of retinoblastoma (Figure 4A, 4B).

2) Orbital tumors The relaxation times in intraorbital tumors are often prolonged (Figure 4C, 4D), even more so in malignant ones. A protracted T₁ produces a lower signal intensity, while an elongated T₂ results in heightened intensity. However, T₁ and T₂ of various tissue-type tumors can considerably overlap. Apart from a few distinctive tumors, discerning based on signal intensity remains challenging. A holistic diagnostic approach is advocated, integrating information on tumor location, extent, morphology, demarcation, and signal intensity^[35-40]. MRI of optic nerve glioma shows that the thickened optic nerve has equal or low signal in the T₁-weighted image, and a high signal in the T₂-weighted image, with uniform enhancement after

enhancement, and sometimes the periphery of the lesion is strengthened and the center is necrotic or cystic^[22]. The tumor is sometimes strengthened at the periphery of the lesion, with necrosis or cystic changes in the center. MRI of meningioma shows that most of the tumors have uniform density, equal or slightly low signal in T₁WI, equal or high signal in T₂WI, uniform and obvious enhancement in enhancement scan, clear boundary, and the meningeal tail sign, *i.e.*, rat-tail enhancement occurs in the meninges adjacent to the tumor^[41] (Figure 4E, 4F).

3) Morphological changes of normal intraorbital structures Changes within the normal orbital framework encompass transformations of the optic nerve, hypertrophy of the extraocular muscles, and thickening of the superior ophthalmic veins. Neoplasms of the optic nerve might manifest as conical, tubular, fusiform, or irregular shapes. Prominent hypertrophy of the extraocular muscles is primarily observed in thyroid-associated orbitopathy and myositic inflammatory pseudotumors (Figure 4G, 4H). In the edematous phase, signals on T₁WI are moderate, while those on T₂WI are intensified. When the lesions undergo fibrosis, both modalities exhibit decreased signals. Enlargement of the superior and inferior ophthalmic veins is predominantly attributed to carotid-cavernous fistulas or thrombophlebitis. The former, characterized by rapid blood flow, eludes detection by gradient

coils, leading to an absent signal in both the cavernous sinus and superior ophthalmic vein on T₁ and T₂-weighted images. Conversely, during the active phase of the latter, T₁WI reveals a moderate signal and T₂WI shows an intensified one.

Other Examination Techniques With the continuous evolution of medical imaging, ophthalmology has incorporated novel imaging modalities like digital subtraction angiography (DSA) and positron emission tomography/computed tomography (PET/CT). DSA operates on the principle of intravenous or arterial contrast administration. Before the contrast medium reaches the orbital region, images are acquired and digitally processed, stored as a subtracted film. A secondary image capture ensues upon the contrast's arrival in the orbit. While the base images primarily capture skeletal and soft tissue details, the subsequent ones also incorporate vascular information from the contrast medium. In the computer system, the latter is subtracted from the former, undergoing digital image transformation to depict the vascular network (Figure 5). By eliminating skeletal overlap, DSA provides enhanced clarity in showcasing ophthalmic arteries, cerebral vasculature, and the vascular supply to orbital tumors. Presently, femoral artery cannulation is widely adopted in DSA, selectively displaying both internal and external carotid arteries, along with vertebral arteries. Selective arteriography is also achievable by guiding the cannula into these vessel branches.

PET/CT revolves around the conversion of fundamental biological elements into positron-emitting radionuclides, subsequently tagging them onto certain compounds. Post-administration, these compounds gravitate towards organs, tissues, or pathological sites with heightened metabolic activity. Once these radionuclides amass internally, their emitted positrons interact with surrounding electrons, resulting in annihilation radiation, generating two antiparallel gamma photons. The PET's crystalline detectors capture these gamma rays, converting them into optical signals relayed to a computer. Following computational processing and reconstruction, sectional images portraying the distribution of these tagged radionuclides are generated. Over the past decade, PET/CT's prowess in discerning cancer metastases and cardiovascular pathologies has solidified its position as an invaluable imaging modality in clinical diagnostics^[42-43].

CONCLUSION

The intricate anatomical composition of the orbit, combined with its close proximity to diverse tissue types, gives rise to a multitude of orbital diseases, presenting diagnostic and therapeutic challenges. The continuous advancements in imaging sciences have consistently revealed innovative diagnostic techniques, enhancing our comprehension of orbital pathologies. While B-scan ultrasonography, CT, and

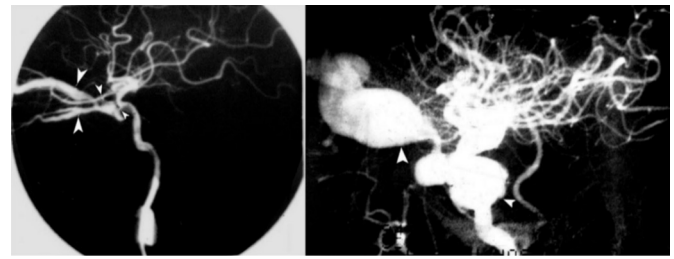


Figure 5 Carotid-cavernous sinus fistula digital subtraction angiography (DSA) shows vessel bulging (arrows).

MRI remain the stalwarts in imaging, the application of three-dimensional ultrasonography, DSA, and PET/CT is burgeoning. Each imaging modality boasts its merits and limitations. To enhance the diagnostic accuracy of various orbital diseases, the judicious selection of appropriate imaging techniques or a multimodal imaging approach can optimize diagnostic efficacy, minimizing the risk of misdiagnoses or miss diagnoses.

ACKNOWLEDGEMENTS

Expert Group Members

Leading authors

Yi Shao	Shanghai General Hospital, Shanghai Jiao Tong University School of Medicine
Jian-Min Ma	Beijing Tongren Hospital, Capital Medical University
Xiao-Ming Huang	Sichuan Eye Hospital
Gang Tan	The First Affiliated Hospital of University of South China
Chong-Gang Pei	The First Affiliated Hospital of Nanchang University
Tong Wu	Sichuan Eye Hospital
Xin-Ji Yang	Chinese People's Liberation Army General Hospital
Xiao-Wei Liu	Peking Union Medical College Hospital
Guang-Yu Li	The Second Norman Bethune Hospital of Jilin University
Li Zhou	The First Affiliated Hospital of Nanchang University
Shi-Ying Li	The First Affiliated Hospital of Xiamen University
Wei Chi	Zhongshan Ophthalmic Center, Sun Yat-sen University
Ming-Zhi Zhang	Joint Shantou International Eye Center (JSIEC) of Shantou University and the Chinese University of Hong Kong
Xuan Liao	Affiliated Hospital of North Sichuan Medical
Liang Hu	Eye Hospital, Wenzhou Medical University; Zhejiang Eye Hospital
Wen-Shi Tao	Bascom Palmer Eye Hospital, USA
Wei-Hua Yang	Shenzhen Eye Hospital
Yan-Wu Xu	South China University of Technology
Wen-Li Yang	Beijing Tongren Hospital, Capital Medical University
Jia Tan	Xiangya Hospital of Central South University
Yao-Hua Wang	Eye Hospital of Nanchang University
Ce Shi	The Second Affiliated Hospital of Zhejiang University
Hui Zhang	The First Affiliated Hospital of Kunming Medical University
Jian-Qi Cai	China National Institute of Standardization
Dan Ji	Xiangya Hospital of Central South University
Jian Ma	The Second Affiliated Hospital of Zhejiang University
Ying Jie	Beijing Tongren Hospital, Capital Medical University
Kai-Jun Li	Shenzhen Eye Hospital

Operation of imaging modalities in orbital diseases

Wen-Qing Shi	Affiliated Tongji Hospital of Tongji University	Qing-Jian Li	Huashan Hospital of Fudan University
Juan Peng	The Second Affiliated Hospital of Guangzhou Medical University	Sheng-Nan Li	Sichuan Eye Hospital
Cheng Li	Eye Institute of Xiamen University	Zheng-Ri Li	Affiliated Eye Hospital of Yanbian University
Guang-Hui Liu	People's Hospital Affiliated to Fujian University of Traditional Chinese Medicine	Zhi-Yuan Li	Chenzhou First People's Hospital
Wen-Jin Zou	The First Affiliated Hospital of Guangxi Medical University	Rong-Bin Liang	Jinshan Hospital of Fudan University
Zhi-Hong Deng	The Third Xiangya Hospital of Central South University	Jing-Wei Lin	Eye Institute of Xiamen University
Yi Liu	Nanjing Hospital of Chinese Medicine Affiliated to Nanjing University of Chinese Medicine	Xiang Lin	Eye Institute of Xiamen University
Xin Wen	Sun Yat-sen Memorial Hospital, Sun Yat-sen University	Zhi-Rong Lin	Xiamen Eye Center of Xiamen University
Lei Tian	Beijing Tongren Hospital, Capital Medical University	Qian Ling	The First Affiliated Hospital of Nanchang University
Hua Liu	The Third Affiliated Hospital of Jinzhou Medical University	Hong-Ling Liu	The First Affiliated Hospital of Harbin Medical University
Xiang-Long Yi	The First Teaching Hospital of Xinjiang Medical University	Qiu-Ping Liu	The First Affiliated Hospital of University of South China
Dan Wen	Xiangya Hospital of Central South University	Sheng-Tao Liu	Eye & ENT Hospital of Fudan University
Zhong-Wen Li	Ningbo Eye Hospital of Wenzhou Medical University	Ting-Ting Liu	Shandong Eye Hospital
Kai Wu	The First Affiliated Hospital of University of South China	Yuan Liu	Bascom Palmer Eye Institute, USA
Sha Wang	Xiangya Hospital of Central South University	Ze-Yu Liu	Eye Institute of Xiamen University
Xiu-Sheng Song	Enshi Clinical College of Wuhan University	Zhao-Lin Liu	The First Affiliated Hospital of University of South China
Qing Zhang	The Second Affiliated Hospital of Anhui Medical University	Zu-Guo Liu	Eye Institute of Xiamen University
Qian-Min Ge	The First Affiliated Hospital of Nanchang University	Shang-Kun Ou	The Affiliated Hospital of Guizhou Medical University
		Jun Ouyang	Jiujiang First People's Hospital
		Kun-Liang Qiu	Joint Shantou International Eye Center (JSIEC) of Shantou University and the Chinese University of Hong Kong
		Rong Rong	Xiangya Hospital of Central South University
		Ting-Ting Shao	Eye & ENT Hospital of Fudan University
		Ting Su	Renmin Hospital of Wuhan University
		Li-Ying Tang	Zhongshan Hospital Xiamen University
		Li-Yang Tong	Ningbo Eye Hospital of Wenzhou Medical University
		Hai-Yan Wang	Shaanxi Eye Hospital
		He Wang	The Affiliated Hospital of Xuzhou Medical University
		Shen Wang	The First Affiliated Hospital of Xinxiang Medical College
		Xiao-Yu Wang	The First Affiliated Hospital of Nanchang University
		Xue-Lin Wang	The First Affiliated Hospital of the Jiangxi Medical College
		Yan Wang	Affiliated Hospital of Inner Mongolia Medical University
		Yi-Xin Wang	Cardiff University, UK
		Hong Wei	The First Affiliated Hospital of Nanchang University
		Yan-Tao Wei	Zhongshan Ophthalmic Center, Sun Yat-sen University
		Jie-Li Wu	Aier Eye Hospital (Changsha)
		Yang Wu	Xiamen Hospital of Zhongshan Hospital Affiliated to Fudan University
		Zhen-Kai Wu	Changde First People's Hospital
		Wei Xia	The First Affiliated Hospital of Soochow University
		San-Hua Xu	The First Affiliated Hospital of Nanchang University
		Yong Yao	C-MER (Guangzhou) Dennis Lam Eye Hospital
		Hai-Jun Yang	Nanchang Puri Eye Hospital
		Qi-Chen Yang	West China Hospital of Sichuan University
		Qing-Hua Yang	Chinese People's Liberation Army General Hospital
		Shu Yang	The First Hospital of Kunming
		Yi-Ran Yang	Henan Provincial People's Hospital
		Yu-Li Yang	The Southwest Hospital of Army Medical University
		Yi-Feng Yu	The Second Affiliated Hospital of Nanchang University
		Yao Yu	The First Affiliated Hospital of Nanchang University
		Qing Yuan	Jiu Jiang No.1 People's Hospital
		Bing Zhang	Hangzhou Children's Hospital
		Yu-Qing Zhang	The Second Affiliated Hospital of Chongqing Medical University

Writing experts

Jing-Hua Bu	Xiang'an Hospital Affiliated to Xiamen University
Yong Chai	Jiangxi Provincial Children's Hospital
Cheng Chen	The First Affiliated Hospital of Nanchang University
Bo Chen	Sichuan Provincial People's Hospital
Jing-Yao Chen	The First Hospital of Kunming
Jun Chen	Jiangxi University of Chinese Medicine
Xin-Jian Chen	Suzhou University
Xu Chen	Maastricht University, Netherlands
Yu Chen	Shanghai University
Zhe Cheng	Aier Eye Hospital (Changsha)
De-Yong Deng	Yueyang Integrated Hospital of Traditional Chinese and Western Medicine Affiliated to Shanghai University of Traditional Chinese Medicine
Yu-Qing Deng	Zhongshan Ophthalmic Center, Sun Yat-sen University
Zhi-Xin Geng	Tianjin MasterVision Technology Co., Ltd., China
Yi Han	Eye Institute of Xiamen University
Liang-Qi He	The First Affiliated Hospital of Nanchang University
Yuan He	The Second Affiliated Hospital of Xi'an Medical College
Jin-Yu Hu	The First Affiliated Hospital of Nanchang University
Shou-Long Hu	Henan Children's Hospital
Cai-Hong Huang	Eye Institute of Xiamen University
Li-Juan Huang	The Second Affiliated Hospital of Fujian Medical University
Ming-Hai Huang	Nanning Aier Eye Hospital
Yong-Zhi Huang	West China Hospital of Sichuan University
Hong-Hua Kang	Eye Institute of Xiamen University
Min Kang	The First Affiliated Hospital of Nanchang University
Ke-Ran Li	Affiliated Eye Hospital of Nanjing Medical University
Ying-Jie Li	The Third Affiliated Hospital of Nanchang University
Juan Li	Shaanxi Eye Hospital
Nai-Yang Li	Zhongshan City People's Hospital

Zhen Zhang	The First Affiliated Hospital of Xiamen University
Yan-Yan Zhang	Ningbo Eye Hospital of Wenzhou Medical University
Hui Zhao	Shanghai General Hospital, Shanghai Jiao Tong University School of Medicine
Yan-Mei Zeng	The First Affiliated Hospital of Nanchang University
Qin-Xiang Zheng	Sir Run Run Shaw Hospital, Zhejiang University School of Medicine
Jing Zhong	Zhongshan Ophthalmic Center, Sun Yat-sen University
Sheng Zhou	Institute of Biomedical Engineering, Chinese Academy of Medical Sciences
Pei-Wen Zhu	Eye & ENT Hospital of Fudan University
Xin-Yue Zhu	Shanghai General Hospital, Shanghai Jiao Tong University School of Medicine
Zhuo-Ting Zhu	The Centre for Eye Research Australia (CERA)
Xin-Yu Zhuang	Joint Shantou International Eye Center (JSIEC) of Shantou University and the Chinese University of Hong Kong
Jie Zou	The First Affiliated Hospital of Nanchang University

Guidelines Statement: All the experts involved in the development of this guideline declare that they adhere to an objective position, based on professional knowledge, research data and clinical experience, and that this guideline is formed after full discussion and unanimous agreement of all the experts. This guideline is drafted by some experts from the Ophthalmic Imaging and Intelligent Medicine Branch of the Chinese Association for Medical Education, Ocular Oncology Committee of the Ophthalmology Branch of the Chinese Medical Doctor Association and the Ophthalmology Specialty Committee of the International Society for Translational Medicine.

Disclaimer: The contents of this guideline represent only the guidance of the experts involved in the development of this guideline for the reference of clinicians. Despite extensive consultation and discussion among experts, there are incomplete points. The recommendations provided in this guideline are not mandatory, and practices that are inconsistent with this guideline do not imply error or inappropriateness. There are still many issues to be explored in clinical practice, and ongoing and future clinical trials will provide further evidence. With the accumulation of clinical experience and the emergence of new treatments, this guideline will need to be revised and updated periodically in the future to bring more clinical benefits to the subjects.

Foundations: Supported by National Natural Science Foundation of China (No.82160195); Jiangxi Double-Thousand Plan High-Level Talent Project of Science and Technology Innovation (No.jxsq2023201036); Key R & D Program of Jiangxi Province (No.20223BBH80014).

Conflicts of Interest: Shao Y, None; Ma JM, None; Huang XM, None; Expert Workgroup of Guidelines for the use of imaging equipment in orbital diseases (2024), None; Ophthalmic Imaging and Intelligent Medicine Branch

Chinese Medicine Education Association, None; Ocular Oncology Committee of the Ophthalmology Branch of the Chinese Medical Doctor Association, None; Ophthalmology Committee of International Association of Translational Medicine, None; Chinese Ophthalmic Imaging Study Groups, None.

REFERENCES

- 1 Li YY, Zhang K, Wang LL, Zhu Y. Analysis of the spectrum of orbital diseases and diagnosis and treatment experiences in large general hospital outpatient service. *Guoji Yanke Zazhi(Int Eye Sci)* 2022;22(7):1234-1238.
- 2 Zhou N, Wei WB. 70 years development of ophthalmic imaging technology in China. *Ophthalmology in China* 2019;28(4):241-244.
- 3 Omatiga AG, Onakpoya OH, Idowu BM, Asaley CM, Adegbehingbe BO, Aderibigbe AS. B-mode sonographic evaluation of optic nerve sheath diameter and lens thickness in Nigerian adults with glaucoma. *Afr Health Sci* 2018;18(2):343-351.
- 4 Gutierrez-Vazquez J, Perez-Sanchez LI, Satrustegui-Lapetra M, Arevalo-Manso JJ, Gomez-Herrera JJ, Criado-Alvarez JJ. Measurement of the anterior chamber depth and ocular axial length: transpalpebral B-mode ultrasound using an 18-MHz linear probe compared with the IOL Master 500. *Med Ultrason* 2021;23(1):48-54.
- 5 Shammas HJ, Wetterwald N, Potvin R. New mode for measuring axial length with an optical low-coherence reflectometer in eyes with dense cataract. *J Cataract Refract Surg* 2015;41(7):1365-1369.
- 6 Yang QH, Chen B, Peng GH, Li ZH, Huang YF. Accuracy of axial length measurements from immersion B-scan ultrasonography in highly myopic eyes. *Int J Ophthalmol* 2014;7(3):441-445.
- 7 Wu ZY, Wang NL, Yang HS. The primary study of ultrasound biomicroscope in imaging anterior segment tumors of eye. *Eye Science* 1997;13(4):189-191.
- 8 Huang Y. Study on anatomy of cavernous sinus and related veins and their application in interventional therapy. *Second Military Medical University* 2017.
- 9 Yu JJ, Liu JX, Wang SJ. Orbital low-dose spiral CT scanning of the clinical research. *Chin J Radiol Health* 2015;24(1):65-66.
- 10 Li H, Jiang RX, Liu YH. A clinical study of B-scan ultrasound examination in the extraocular muscles for thyroid-associated ophthalmopathy. *Chinese Journal of Medical Imaging Technology* 2008;24(11):1737-1739.
- 11 Mo F, Li H. Advances in imaging research of thyroid associated ophthalmopathy. *Chinese Journal of Medical Ultrasound (Electronic Edition)* 2020;17(8):795-799.
- 12 Liang XF, Chen ZF. Application of color Doppler ultrasound in the diagnosis and treatment of thyroid-related eye diseases. *Chinese Journal of Control of Endemic Diseases* 2017;32(8):909-910.
- 13 Xu BH, Zeng Q, Wei LL, et al. Real-time continuous microvascular superposition method under contrast-enhanced ultrasound for reconstructing blood vessels of breast tumors. *Chinese Journal of Medical Imaging Technology* 2023;39(10):1571-1574.

- 14 Shen L, Jiang SG, Wang H, *et al.* Clinical application of low-dose spiral CT scan of the orbit. *Journal of Practical Medical Techniques* 2012;19(11):1155-1156.
- 15 Wang D. CT evaluation of traumatic carotid-cavernous fistula. *Journal of Medicine Tribune* 2008;29(21):83-84.
- 16 Xiao LH. Modern imaging diagnosis of orbital disease. *Ophthalmology in China* 2001;10(2):66-70.
- 17 Wang ZC, Xian JF, Shi DP, *et al.* *Head and neck imaging: Ophthalmology volume*. Beijing: People's Medical Publishing House, 2014:1-25.
- 18 Xian JF, Wang ZC, Yang BT. Innovation and standardization of head and neck CT and MRI examinations to improve diagnosis and research. *Radiology Practice* 2011;26(3):246-247.
- 19 Yang R, Dai LM, Li JY, *et al.* Application of multislice spiral CT low-dose scanning in the examination of orbital trauma. *Chinese Journal of Radiology* 2010;44(7):731-734.
- 20 Editorial Committee of Chinese Journal of Radiology. Guidelines for the standardization of head and neck CT and MR scans (revised). *Chinese Journal of Radiology* 2007;41(9):996-999.
- 21 Working Group on the Safe Use of Contrast Agents of the Radiology Branch of the Chinese Medical Association. A guide to the use of iodine contrast media (2nd ed.). *Chinese Journal of Radiology* 2013;47(10):869-872.
- 22 Xu QG. Tumor-associated optic neuropathy. *Chinese Journal of Ophthalmology and Otorhinolaryngology* 2022;22(1):3-6.
- 23 Song C, Tian F, Wan YL, *et al.* Clinical application value of multi-slice spiral CT in the diagnosis of ocular trauma. *Modern Medical Imageology* 2023;32(8):1516-1518.
- 24 Tanenbaum RE, Lobo R, Kahana A, Wester ST. Advances in magnetic resonance imaging of orbital disease. *Can J Ophthalmol* 2022;57(4):217-227.
- 25 Chen Y, Xiang CQ, Liu WF, Jiang N, Zhu PW, Ye L, Li B, Lin Q, Min YL, Su T, He LC, Shao Y. Application of amplitude of low-frequency fluctuation to altered spontaneous neuronal activity in classical trigeminal neuralgia patients: a resting-state functional MRI study. *Mol Med Rep* 2019;20(2):1707-1715.
- 26 Xu MW, Liu HM, Tan G, Su T, Xiang CQ, Wu W, Li B, Lin Q, Xu XW, Min YL, Liu WF, Gao GP, Shao Y. Altered regional homogeneity in patients with corneal ulcer: a resting-state functional MRI study. *Front Neurosci* 2019;13:743.
- 27 Huang X, Li HJ, Ye L, Zhang Y, Wei R, Zhong YL, Peng DC, Shao Y. Altered regional homogeneity in patients with unilateral acute open-globe injury: a resting-state functional MRI study. *Neuropsychiatr Dis Treat* 2016;12:1901-1906.
- 28 Ye L, Wei R, Huang X, Shi WQ, Yang QC, Yuan Q, Zhu PW, Jiang N, Li B, Zhou Q, Zhou FQ, Shao Y. Reduction in interhemispheric functional connectivity in the dorsal visual pathway in unilateral acute open globe injury patients: a resting-state fMRI study. *Int J Ophthalmol* 2018;11(6):1056-1060.
- 29 Tang LY, Li HJ, Huang X, Bao J, Sethi Z, Ye L, Yuan Q, Zhu PW, Jiang N, Gao GP, Shao Y. Assessment of synchronous neural activities revealed by regional homogeneity in individuals with acute eye pain: a resting-state functional magnetic resonance imaging study. *J Pain Res* 2018;11:843-850.
- 30 Shen J, Xu XQ, Hu H, Liu H, Shi HB. The value of conventional MRI combined with diffusion weighted imaging in the differential diagnosis of orbital lymphoproliferative disorders. *Chinese Journal of Radiology* 2016;50:412-415.
- 31 Kuai XP, Wang SY, Tao XF. Application of magnetic resonance diffusion-weighted imaging in orbital lesions. *Radiology Practice* 2013;28(6):692-694.
- 32 Kuai XP, Wang SY, Liu SY, *et al.* Value of diffusion-weighted imaging in the diagnosis of orbital lymphoma. *Chinese Journal of Radiology* 2013;47(6):490-494.
- 33 He LY, Xian JF, Wang ZC, *et al.* The conventional and dynamic contrast-enhanced MR imaging findings of lymphoma of the orbit. *Chinese Journal of Radiology* 2007;41(9):918-921.
- 34 Tao XF, Wan WP, Xiao XS, *et al.* The diagnosis of orbital tumor with dynamic contrast-enhanced MRI. *Chinese Journal of Radiology* 2006;40(4):360-364.
- 35 Zhao X, Xu D, Li SH, *et al.* Imaging signs of orbital tumors and tumorlike lesions in MRI and their differential diagnosis study. *Chinese Journal of CT and MRI* 2022;20(8):47-49.
- 36 Li F, Liu K, Sun GL. The value of conventional MRI combined with apparent diffusion coefficient in differential diagnosis of orbital tumors. *Chinese Journal of Magnetic Resonance Imaging* 2020;11(12):1163-1166.
- 37 Liu YN, Gao YX, Shu HY, Li QY, Ge QM, Liao XL, Pan YC, Wu JL, Su T, Zhang LJ, Liang RB, Shao Y. Altered brain network centrality in patients with orbital fracture: a resting-state functional MRI study. *Exp Ther Med* 2023;26(6):552.
- 38 Kang M, Gao YX, Zhang LJ, Liang RB, Li QY, Shu HY, Pan YC, Ying P, Xu SH, Yi S. Detection of abnormal spontaneous brain activity patterns in patients with orbital fractures using fractional amplitude of low frequency fluctuation. *Front Neurol* 2022;13:874158.
- 39 Song GX. Qualitative diagnosis of orbital tumors by ultrasound, CT and MRI and orbital cavity repair after orbital content resection. *The Second Hospital of Tianjin Medical University* 2006-01-01.
- 40 Chen ZH, Chen RZ, Situ MT, *et al.* Imaging analysis and differential diagnosis of meningioma. *Chinese Journal of CT and MRI* 2020;18(2):54-56.
- 41 Wang RF, Li XF, Zhang CL. Progress and clinical application of PET/CT. *China Medical Device Information* 2007;13(7):1-4,14.
- 42 Bomanji J, Costa D, Ell P. Clinical role of positron emission tomography in oncology. *Lancet Oncol* 2001;2(3):157-164.
- 43 Endo K, Oriuchi N, Higuchi T, Iida Y, Hanaoka H, Miyakubo M, Ishikita T, Koyama K. PET and PET/CT using 18F-FDG in the diagnosis and management of cancer patients. *Int J Clin Oncol* 2006;11(4):286-296.